Thermal behavior of regolith at cold traps on the moon's south pole: Revealed by Chang'E-2 microwave radiometer data

Guangfei Wei [a], Xiongyao Li [a,*], Shijie Wang [b]

[a] Center for Lunar and Planetary Sciences, Institute of Geochemistry, Chinese Academy of Sciences, Guiyang 550081, China
[b] State Key Laboratory of Environmental Geochemistry, Institute of Geochemistry, Chinese Academy of Sciences, Guiyang 550081, China

ABSTRACT

The long-term stability of water ice at cold traps depends on subsurface temperature and regolith thermophysical properties. Based on Chang'E-2 microwave radiometer data, we have inverted attenuation coefficient, thermal gradient and instantaneous temperature profiles at permanently shaded craters (Cabeus, Haworth and Shoemaker) on the Moon's south pole. The nonuniformity of the inverted attenuation coefficient within the craters reflects the inhomogeneous thermophysical properties of regolith. In addition, thermal gradient decreased significantly from the crater walls to the bottoms, which may be caused by scattered sunlight, internal heat flux and earthshine effect. Considering continuous supplement of water ice (with volumetric fraction 0–10%) at cold traps, it changes subsurface thermophysical properties but has little effect on thermal gradient. We also assumed that abundant ice (10%) mixed with regolith, the inversion results showed that the maximum difference of diurnal temperatures between "wet" and dry regolith were no more than 0.5 K. That is, the effect of water ice on subsurface thermal behavior can be neglected.

© 2016 Elsevier Ltd. All rights reserved.

1. Introduction

Cold traps at the Moon's south polar region are the most fascinating and important destinations for lunar explorations in search of water and sites for future human colonization. Due to small oblique angle of the Moon's spin axis with respect to ecliptic (1.54°), the plausibility of existence of water ice in cold traps was initially discussed by Watson et al. (1961). Cold traps favorably harbor water ice that originates from occasional comets, water-containing meteorites, and solar-wind-induced iron reduction of regolith; yet ice is lost due to solar wind sputter erosion (Arnold, 1979; Crider and Vondrak, 2002, 2003; Klumov and Berezhnoi, 2002). The processes of deposition and sublimation in these regions have been sustained for nearly 2 Gyr, since the Moon's orbital evolution became stable (Arnold, 1979; Bills and Ray, 1999).

Both radar experiments and neutron spectrometer readings have implied that water ice is concentrated at cold traps in lunar south polar regions (Nozette et al., 1996; Feldman et al., 1998; Mitrofanov et al., 2010). Recently, hydroxyl and water have been founded to focus in polar regions by global scale infrared detection in three separate missions, Cassini (Clark, 2009), Chandrayaan-1 (Pieters et al., 2009) and Deep Impact (Sunshine et al., 2009). In

addition, the presence of water ice was confirmed later by impact experiment at Cabeus crater using observations of near-infrared and ultraviolet/visible spectrometers onboard the Lunar Crater Observation and Sensing Satellite (LCROSS) (Colaprete et al., 2010; Schultz et al., 2010).

Indeed, the stability of water ice at cold traps is predominantly controlled by thermal behavior of lunar regolith (e.g., Salvail and Fanale, 1994; Lucey et al., 2004; Schorghofer and Taylor, 2007; Paige et al., 2010b; Siegler et al., 2011; Schorghofer and Aharonson, 2014). Thermal regime within these regions are governed by regolith thermophysical properties, topographically-driven scattered sunlight, surface thermal re-radiation, internal heat flows and earthshine (Paige et al., 2010b; Sefton-Nash et al., 2013; Siegler et al., 2015). Water molecules can also be enhanced in excess of surface concentration by pumping effect due to temperature cycle, and the ice would become thermal immobile once the maximum temperatures dropped below ~100 K (Schorghofer and Aharonson, 2014; Siegler et al., 2015). For the continuous ice delivering and space weathering at cold traps in the Moon's geologic history, thermal behavior of the ice regolith mixture may become complex.

Recently, lunar surface thermal radiation and regolith thermophysical properties are investigated by Diviner Lunar Radiometer Experiment (Diviner) onboard Lunar Reconnaissance Orbiter, especial for lunar south polar regions (Paige et al., 2010b; Vasavada et al., 2012). The Diviner experiment is designed to

observe lunar global thermal environment. It contains two spectral channels for reflected solar radiation (each 0.35–2.8 μm) and seven channels for surface infrared emission (ranging 7.55–400 μm) (Paige et al., 2010a). At a low polar orbit 50 km, Diviner observes lunar surface with spatial resolution of ∼200 m and an image swath of 3.4 km. Based on repeat coverage of Diviner observations at polar regions, cryogenic regions are identified and the locations where water ice might be cold trapped are investigated (Paige et al., 2010b). However, for the shallow penetration depth of thermal infrared, regolith thermal behavior and thermophysical properties at greater depths cannot be revealed directly by observed data.

Chang'E-2 (CE-2), China's second lunar probe, was launched on October 1, 2010. Microwave radiometer (MRM) onboard CE-2 is the same as its predecessor onboard Chang'E-1 (CE-1) which has four channels: 3.0, 7.8, 19.35, and 37 GHz (Fang and Fa, 2014). For the lower altitude of CE-2, approximately 100 km, the spatial resolution increases to 15 km (the 3.0 GHz channel has a resolution of 25 km), and the radiometric accuracy is 0.5 K. During the operation period of MRM for more than six months in a polar orbit, repeat coverage of brightness temperature (Tb) data at polar regions are obtained. Regarding the sensitivity of passive microwave to the subsurface, the regolith becomes more transparent for longer wavelengths. Therefore, the MRM is able to examine greater depths, and it is feasible to reveal subsurface thermal behavior and regolith thermophysical properties at cold traps (Zheng et al., 2012). Thus, it is necessary to build a microwave radiative transfer model that combines thermal parameters with MRM observations. Here we select Tb data at 37 (Tb_{37}) and 19.35 (Tb_{19}) GHz to retrieve subsurface thermal behavior at cold traps because the two channels are sensitive to temperature variations from surface to ∼1 m depth.

In Section 2, we first employed a time- and depth-dependent temperature model. Then the mixture dielectric constant of "wet" regolith (mixed with water ice) was calculated. To derive thermal parameters from high frequency Tb data, a least square method was introduced. Selecting the data sets of Tb_{37} and Tb_{19} covering permanently shaded craters (Cabeus, Haworth and Shoemaker), the attenuation coefficient, thermal gradient and instantaneous temperature profiles were inverted in Section 3. In Section 4, we validated our inversion results and discussed the inversion uncertainty. Finally, we summarized our work and gave the conclusion in Section 5.

2. Method

2.1. Temperature model

Both Apollo 15 and 17 heat flow measurements indicate a low conductivity dust layer that is about 2 cm thick covering the more compacted lunar soil (Keihm et al., 1973). Thus, the one-dimensional thermal model including dust and regolith layers was widely used to investigate regolith thermal behavior from equatorial zone to polar regions (Vasavada et al., 1999, 2012; Paige et al., 2010b). However, it is difficult to accurately simulate subsurface temperature at cold traps because regolith thermophysical properties and interior heat flux are not well constrained, especially at greater depths (> 10 cm) (Paige et al., 2010b).

It is worth noting that although the cold traps are shaded from sunlight, they still are warmed by receiving scattered solar energy, thermal emission from surrounding topography, earthshine and internal heat flux (Vasavada et al., 1999; Paige et al., 2010b). Accordingly, thermal behavior of cold traps also varies as responding to the changes of above heat sources. For example, we collected Tb_{37} data points covering the bottom of Cabeus, Haworth
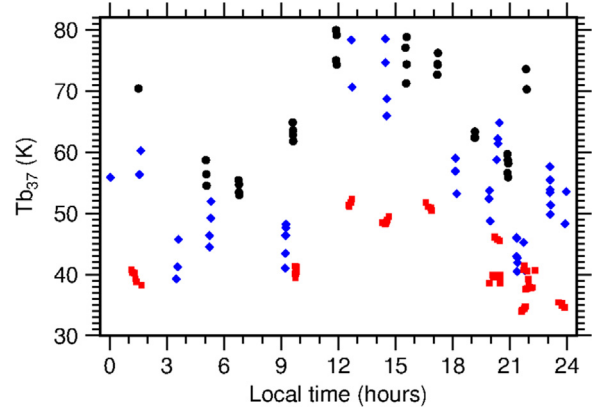

Fig. 1. Tb_{37} at the bottom of different craters varies with local times. The black points, blue diamonds and red squares denote the data covering Cabeus ($36° - 34.2°W$; $84.8° - 85°S$), Haworth ($3° - 4.9°W$; $86.8° - 87°S$) and Shoemaker ($43.9° - 45.9°E$; $88.0° - 88.2°S$), respectively. (For interpretation of the references to color in this figure caption, the reader is referred to the web version of this paper.)

and Shoemaker craters, and found that they still vary with local times in a small but a distinguished fluctuation (as shown in Fig. 1).

As Tb varies with local time periodically, the time- and depth-dependent temperature can be simulated by Fourier series (Wesselink, 1948; Mezger and Strassl, 1959). Considering heat flux from lunar interior, the temperature model can be written as

$$T(t,z) = T_m + T_a \exp(-\beta z) \cos(\omega t - \beta z) + gz \tag{1}$$

where T_m is mean subsurface temperature, T_a is temperature amplitude, β is attenuation coefficient, ω is angular frequency, t is local time, z is depth, and g is thermal gradient.

2.2. Inversion approach

As indicated by Apollo 17 in situ heat flow measurement, diurnal temperatures decrease drastically with depth in upper layer (< 15 cm) of regolith (Keihm and Langseth, 1973). In order to accurately simulate the temperature profile, we built an inhomogeneous multi-layer model in which the thickness of layer increased with depth exponentially. Thus, more discrete temperature points corresponding to the layers are distributed near the surface. For the nadir viewing of CE-2's MRM (the observation angle equals zero), the contribution of Tb from each layer can be expressed by Eq. (2) based on fluctuation dissipation theory (Jin, 1984; Zhou et al., 2010):

$$Tb_i = \left(1 - e^{-2k_i^{"}d_i}\right)\left(1 + |R_{i(i+1)}|^2 e^{-2k_i^{"}d_i}\right) \prod_{j=0}^{i-1}\left[\left(1 - |R_{i(i+1)}|^2\right)e^{-2k_j^{"}d_j}\right]T_i \tag{2}$$

Additionally, the contribution of Tb from the bottom layer (Tb_n) can be written as (Jin, 1984; Zhou et al., 2010)

$$Tb_n = \prod_{j=0}^{n}\left[\left(1 - |R_{j(j+1)}|^2\right)e^{-2k_j^{"}d_j}\right]T_n \tag{3}$$

Finally, the total contributions of Tb from the multi-layer can be summed up as follows:

$$Tb = k_0 \sum_{i=1}^{n-1} \frac{\varepsilon_{ri}^{"}}{2k_{iz}^{"}}\left[1 - e^{-2k_{iz}^{"}d_i}\right]$$

$$\cdot \left[1 + |R_{i(i+1)}|^2 e^{-2k_{iz}^{"}d_i}\right] \prod_{j=0}^{i-1}\left[|X_{j(j+1)}|^2 e^{-2k_{iz}^{"}d_i}\right]T_i$$

$$+ \frac{k_0 \varepsilon_{rn}^{"}}{2k_{nz}^{"}}|X_{j(j+1)}|^2 e^{-2k_{jz}^{"}d_j} \prod_{j=0}^{n-1}\left[|X_{j(j+1)}|^2 e^{-2k_{iz}^{"}d_i}\right]T_n \tag{4}$$

where n is layer number, ε_{ri} ($i = 1, \ldots, n$) is relative dielectric constant, k_0 is wave number of free space, k_{iz} is wave number along z direction of i-th layer, and k_{iz}'' is imaginary part of k_{iz}. $R_{i(i+1)}$ and $X_{i(i+1)}$ are reflection coefficient and transmission coefficient between i-th and $(i+1)$-th layers, respectively. d_i and T_i are thickness and temperature of the i-th layer, respectively. Note that T_i can be calculated from Eq. (1).

To calculate Eq. (4), we should obtain the dielectric constant of each layer. Terrestrial measurement of Apollo samples shows that ε_r is a function of bulk density (ρ) and (FeO+TiO$_2$) content (S, in percentage). It can be expressed as (Heiken et al., 1991)

$$\varepsilon' = 1.919^{\rho} \tag{5a}$$

$$\tan \delta = 10^{0.038S + 0.312\rho - 3.26} \tag{5b}$$

where $\tan \delta = \varepsilon''/\varepsilon'$ is loss tangent. ε' and ε'' are real and imaginary parts of dielectric constant, respectively. In addition, terrestrial measurement also shows that the bulk density of regolith is related to its buried depth (z, in meters), and the formula can be written as (Heiken et al., 1991)

$$\rho(z) = 1.919 \frac{z + 0.122}{z + 0.18} \tag{6}$$

It is worth noting that the dielectric constant of "wet" regolith (mixed with ice) at cold traps becomes complex, and it depends on the ice content (w_{ice}) and regolith textural composition. Analysis of neutron data from Lunar Prospector spectrometer indicates that ice confined to the permanently shaded craters appears to be mixed in with regolith at 1% of weight fraction (Feldman et al., 2000). Thus, the volume fraction of ice mixed with regolith is approximately to 3%. Formulae of mixture dielectric constant are examined by Reynolds and Hough (1957), and Shutko and Reutov (1982) reduced them to six basic ones. Comparisons of these models for calculating "wet" regolith dielectric constant are discussed in detail by Meng et al. (2010). Here, we applied the Clausius model (matrix) to calculate the mixture dielectric constant (ε_m). The model for calculating mixture dielectric constant can be written as follows (Shutko and Reutov, 1982):

$$\varepsilon_m = \varepsilon_{reg} \times \left(1 + \frac{w_{ice}}{\frac{1 - w_{ice}}{3} + \frac{\varepsilon_{reg}}{\varepsilon_{ice} - \varepsilon_{reg}}}\right) \tag{7}$$

where ε_{reg} and ε_{ice} are dielectric constant of regolith and ice, respectively. w_{ice} denotes the volumetric fraction of ice.

As an example shown in Fig. 2, it presents apparent different dielectric constant profiles that are mixed with (blue lines) and without (black lines) water ice. Both the dry and "wet" regolith dielectric constant increase with depth gradually. However, the real part of dielectric constant (solid lines) decreases after mixing with ice. On the contrary, the imaginary part of mixed dielectric constant (dashed lines) increases notably comparing to the dry regolith. Thus, the fraction of ice mixed with regolith may play a part in Tb simulations and inversion results.

To avoid an ill-posed inversion problem, a least square method (Eq. (8)) was employed by minimizing the Tb differences between simulations in Eq. (4) and CE-2 observations Tb^o (the superscript "o" denotes the observed value). Therefore, Eq. (1) can be solved by searching the most appropriate values of T_m, T_a, β and g:

$$T_m, T_a, \beta, g = \arg \min \left[(Tb_{37} - Tb_{37}^o)^2 + (Tb_{19} - Tb_{19}^o)^2\right] \tag{8}$$
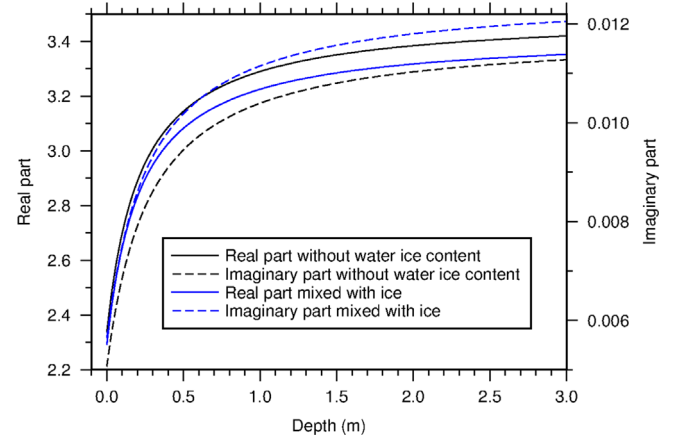

Fig. 2. Shown is dielectric constant as a function of depth which is mixed with (blue lines) and without (black lines) water ice. The solid and dashed lines denote real (left Y-axis) and imaginary parts (right Y-axis) of dielectric constant, respectively. Note that the mixed volumetric fraction of water ice is 10%, and the dielectric constant is given as $\varepsilon_{ice} = 3.2(1 + 0.0035i)$ (Meng et al., 2010). (For interpretation of the references to color in this figure caption, the reader is referred to the web version of this paper.)

3. Results

3.1. Thermal characteristics revealed by Tb

Based on repeated coverage of microwave radiometer observations at south polar region, we collected Tb data at 37 and 19.35 GHz (the CE-2 MRM data set were valid between November 1, 2010 and May 20, 2011) and averaged them by 3×3 km^2 bins. Fig. 3 (right panel) shows the daytime brightness temperature at 37 GHz of lunar south pole ($\geq 80°$S). We also selected the channel 8 of Diviner data near noontime that covered the same range with CE-2 data. For the sake of facilitate comparison, the Diviner data were also binned by 3×3 km^2 as shown in Fig. 3 (left panel). Obviously, the extreme cold patches including Cabeus (a), Haworth (b) and Shoemaker (c) craters characterized by Tb$_{37}$ are very consistent with the surface cryogenic regions and low rate illumination areas (Noda et al., 2008). These cold patches were also identified by CE-1 MRM data under lower spatial resolution (Chan et al., 2010). In addition, distribution of Tb$_{19}$ also presents similar thermal feature as well as Tb$_{37}$ at polar regions.

Comparing to Tb$_{37}$, the microwave at 19.35 GHz penetrates greater depth because of its longer wavelength. Here, we collected daytime Tb$_{37}$ and Tb$_{19}$ data points that covering polar regions ($\geq 80°$S) for comparison. Fig. 4 shows the data density cross plot of brightness temperature, i.e., Tb$_{37}$ vs. Tb$_{19}$. The low temperature data family points enclosed by ellipse consist of cryogenic regions that are shaded from solar illumination. It indicates greater thermal regime in deeper depths at cold traps.

3.2. Subsurface thermal behavior

In order to characterize and compare subsurface thermal behavior at different cold traps, we selected the Cabeus, Haworth and Shoemaker craters as study areas (which are labeled in Fig. 3). We first filtered the Tb$_{37}$ and Tb$_{19}$ data sets by 3×3 km^2 bins and calculated the mean value of each square. Then, it is essential to obtain (FeO+TiO$_2$) content at these craters before calculating the mixture dielectric constant by Eqs. (5)–(7). Up till now, gamma ray spectroscopy data from Lunar Prospector have been used to retrieve the global content of elements, such as Fe and Ti (Prettyman et al., 2006). Under the rough resolution of $2° \times 2°$, the fraction of (FeO+TiO$_2$) at Cabeus, Haworth and Shoemaker is retrieved approximately to 5% each (Prettyman et al., 2006).
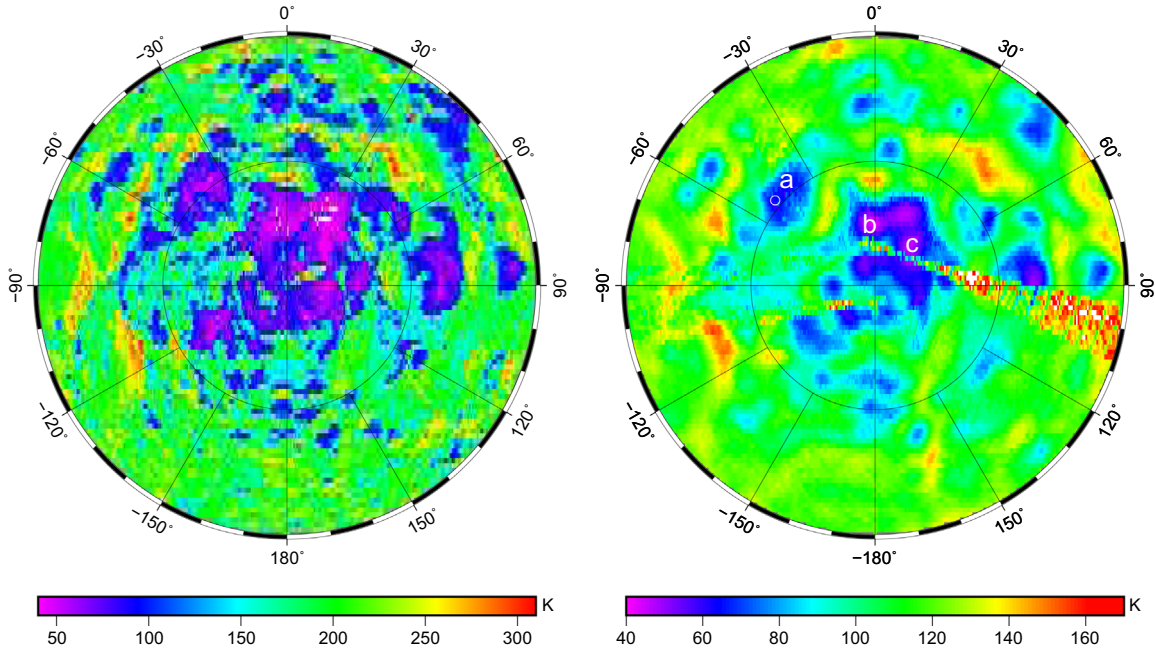
Fig. 3. Mosaic of noontime infrared temperature that is derived from channel 8 of Diviner data (left panel) and daytime Tb$_{37}$ (right panel) confined to the lunar south polar region ($\geq 80°$ S). a, b and c denote the craters of Cabeus, Haworth and Shoemaker. The white circle denotes the LCROSS impact site (49.6°W, 84.7°S). Note that the wedge area of right panel indicates data missing and is interpolated from nearest area. They are mapped under polar stereographic projection.
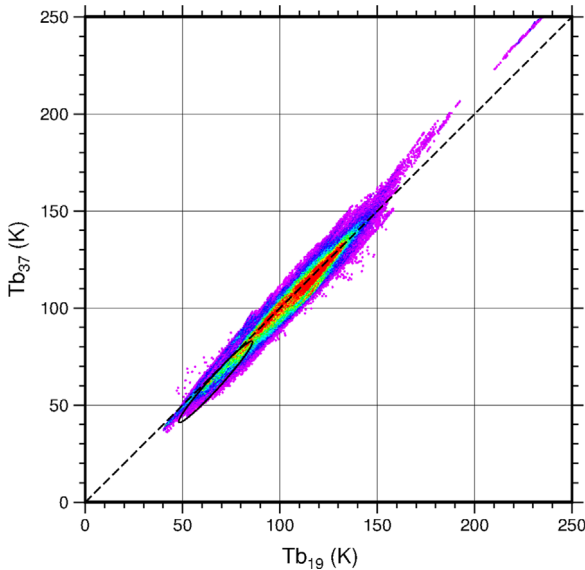

Fig. 4. Data density cross plot of daytime brightness temperatures at 37 and 19.35 GHz that are confined in lunar south polar regions ($\geq 80°$S). The data family points enclosed by ellipse indicate extreme low temperature regions locating at cold traps as presented in Fig. 3.

As shown in Fig. 5a, c, e, the distributions of attenuation coefficient at the craters are nonuniform. It indicates that heat flux transfers into and out of surface at the cold traps inhomogeneously. This may be related to nonuniform regolith thermophysical properties. Comparing to Haworth and Shoemaker, regolith of Cabeus with relative greater attenuation coefficient corresponds to shallower thermal skin depth (λ_D) from the relation $\lambda_D = 1/\beta$. However, thermal gradient varies drastically from 3.0 to 0.5 K/m among the cryogenic areas (as shown in Fig. 5b, d and f). Considering the mean thermal gradient, it is greater in Cabeus than that of Haworth and Shoemaker. Note that the inverted thermal gradient decreases significantly from the walls to the bottoms. This

may be caused by scattered sunlight or earthshine in addition to heat flow from interior.

For the inhomogeneous thermophysical properties of regolith within the craters, as an example, we presented instantaneous temperature profiles near the center of craters for comparison. As shown in Fig. 6, it is obvious that diurnal variation of surface temperature propagates downward to a greater depth of about 1 m below surface. The different surface temperature amplitudes among the study areas indicate that they receive different scattered sunlight and earthshine in a lunar cycle. The linear increase of temperatures in the form of different thermal gradients (g) correspond to different magnitude of heat flows. Here, the heat flow (F) can be estimated from the relation $F = \kappa \partial T / \partial z = \kappa g$, where κ is thermal conductivity, and we derived it from the relation $\kappa = \kappa_c \left[1 + \chi (T/350)^3 \right]$ following the work of Paige et al. (2010b). Thus, heat flows near the bottoms of Cabeus and Haworth are estimated to be 11.2 mW/m^2, and 7.4 mW/m^2 for Shoemaker. This may provide some constraints on internal heat flows in addition to radioactive elements within these cold traps.

4. Discussions

4.1. Inversion validations

Since there is no direct measurement of temperature profile at the permanently shaded craters, we tried to compared our inversion results at LCROSS impact site with theoretical simulation as in the work of Paige et al. (2010b). As shown in Fig. 7 (blue lines), the maximum and minimum temperatures in 500 m scale vary drastically with depth in the top 2 cm thick dust layer. The profile features are different with our inversion results (black lines) because of different temperature models. However, it presents similar temperature amplitudes at surface and similar propagation trend at greater depths. Note that the inverted heat flow at LCROSS impact site was estimated to be about 10 mW/m^2 from the relation $F = \kappa \partial T / \partial z$.
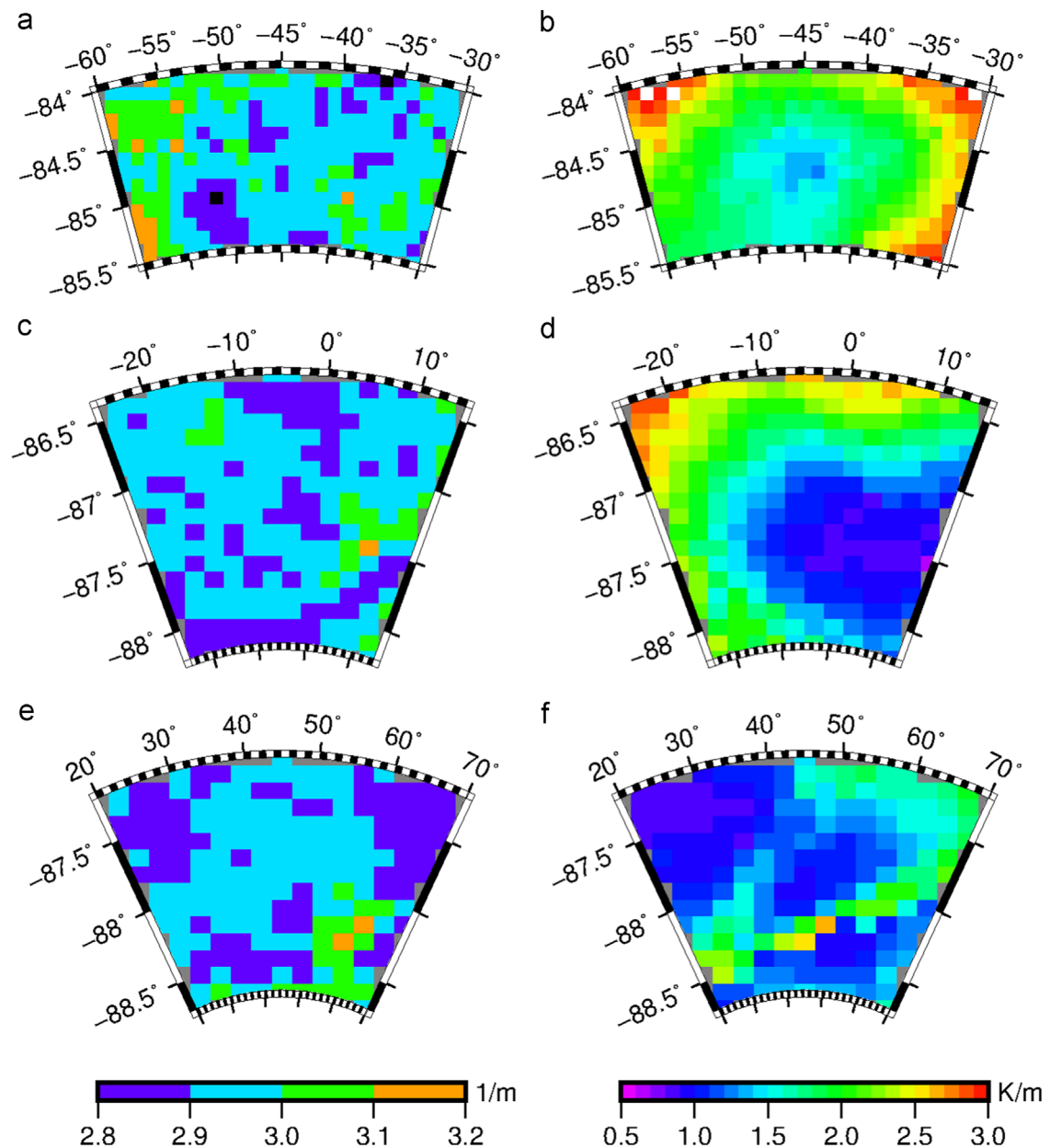
Fig. 5. Shown are inverted attenuation coefficient and thermal gradient at Cabeus (a, b), Haworth (c, d) and Shoemaker (e, f). The left column is inverted attenuation coefficient, and the right column is inverted thermal gradient. Figures are mapped under conic projection.

Based on repeated global coverage of Diviner data, it provides a good constraint for diurnal temperature variation at any point of the Moon. Here, we collected thermal infrared observations from channel 8 of Diviner that covering LCROSS impact site (labeled by white circle in Fig. 3) from December 1, 2010 to November 30, 2012. Fig. 8 (blue dots) shows the diurnal variation of surface temperature (here, we assume the infrared emissivity to be 1 for simplification). It presents a good consistent with our inverted surface temperature (black line) from midnight to 08:00. The temperature difference during the daytime may be caused by scattered sunlight.

4.2. Inversion uncertainty

As noted above, the content of water ice affects the mixture dielectric constant (as shown in Fig. 2). However, the mixed fraction of ice at cold traps is not determined in large scale, and this also makes thermophysical properties of the mixture uncertain. To discuss the inversion uncertainty resulting from ice content, we first selected the data sets of Tb_{37} and Tb_{19} near the bottom of Cabeus, Haworth and Shoemaker. Then, the attenuation coefficient and thermal gradient were inverted under different fractions of ice. It is worth noting that dielectric constant of water ice is also temperature dependent while their mathematical relation at extreme low temperature is undetermined (Evan, 1965). For the relatively stable thermal regime at cryogenic craters, we neglect the temperature effect and pay more attention to the effect of ice content.

As shown in Fig. 9, both attenuation coefficient and thermal gradient vary with the increase of ice content. That is, thermal behavior of regolith is related to the mixed fraction of ice. It is apparent that thermal gradient increases slightly (about 0.6%–0.8%) with the increase of volumetric fraction of ice (from 0% to 10%). However, thermal attenuation varies from 4% to 6%. It suggests that continuous supplement of water ice at the cryogenic
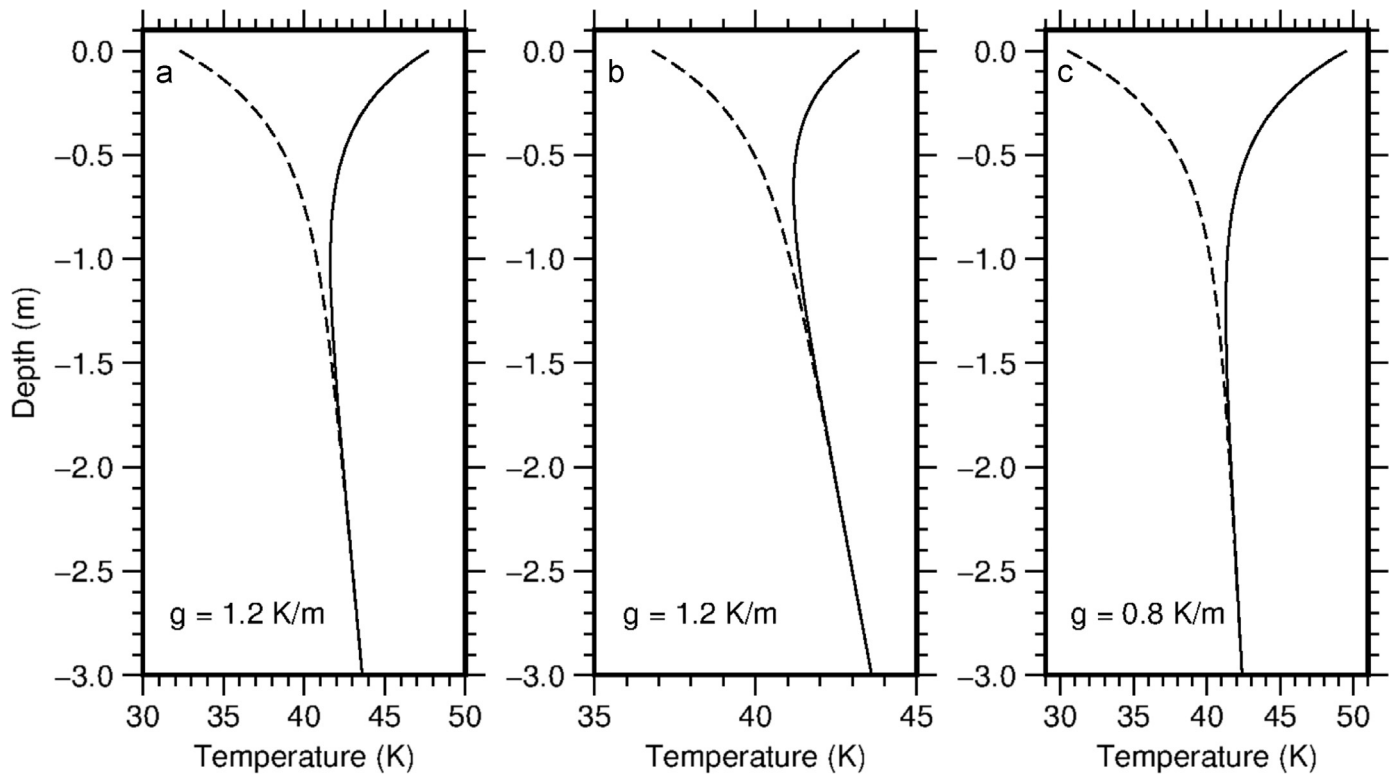
Fig. 6. Inverted instantaneous temperature profiles near the center of Cabeus (a, 45.1°W, 84.9°S), Haworth (b, 5.1°W, 87.0°S) and Shoemaker (c, 45.0°E, 88.1°S). The dashed and solid lines denote the minimum and maximum instantaneous temperature profiles, respectively. The mixed volumetric fraction of water ice was given as 3%.
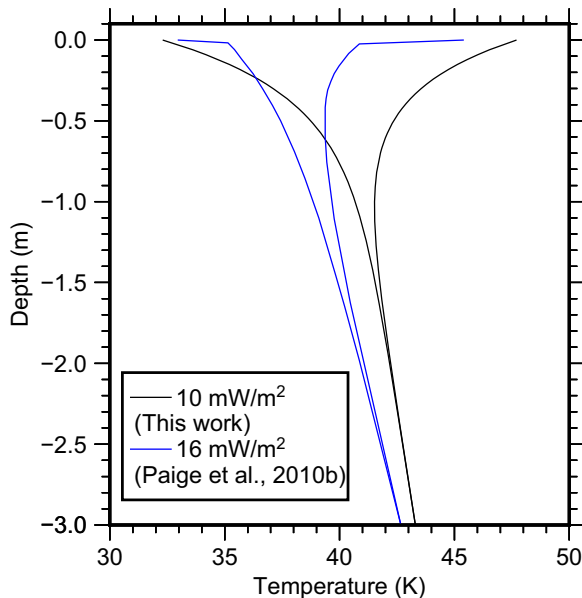

Fig. 7. Comparison of maximum and minimum temperature profiles at LCROSS impact site. The blue lines are reproduced from the work of Paige et al. (2010b) when given the internal heat flow for 16 mW/m². The black lines are inverted results which correspond to the heat flow of 10 mW/m². (For interpretation of the references to color in this figure caption, the reader is referred to the web version of this paper.)

Fig. 8. Surface (infrared brightness) temperature varies with local time at LCROSS impact site. The blue dots denote infrared brightness temperatures that are derived from channel 8 of Diviner. The black curve denotes inverted surface temperature. (For interpretation of the references to color in this figure caption, the reader is referred to the web version of this paper.)

regions affects the subsurface thermal behavior but has little effect on thermal gradient.

To compare the subsurface temperature as a result of different amount of ice delivered at cold traps. Here, we considered two conditions: (1) there is no ice that is delivered at the cold traps, namely pure dry regolith; (2) the regolith mixed with 10% volume of ice, i.e., very "wet" reg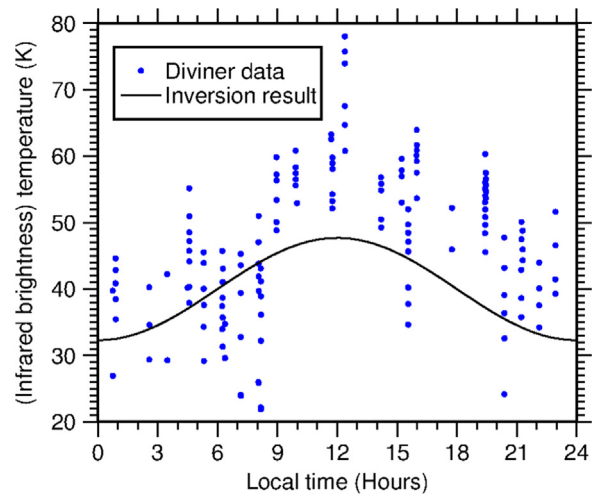olith. Then the differences of maximum and minimum temperatures between the "wet" and dry regolith at Cabeus, Haworth and Shoemaker were calculated, respectively. As shown in Fig. 10, the temperature differences vary significantly in shallow depth (0–0.3 m). However, notably, the temperature differences at all depths are so small (no more than 0.5 K) that they can be ignored. Thus, thermal emission at cold traps observed by microwave radiometer onboard CE-1 and CE-2 mainly depends on the thermophysical properties of ice harboring regolith.

It is also necessary to discuss inversion uncertainty if observed Tb was brought by some noises. Because the radiometric resolution of MRM is 0.5 K, we assumed that a noise $\pm$ 0.5 K was added
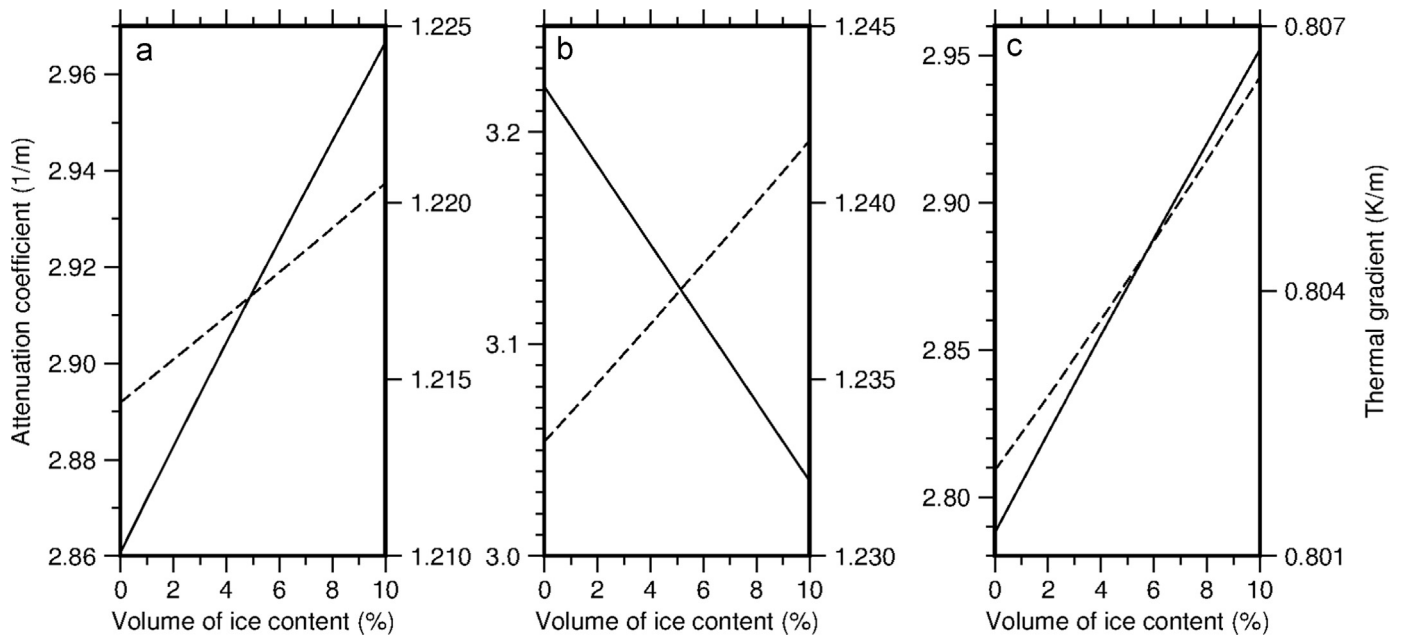
Fig. 9. Effect of ice fraction on attenuation coefficient and thermal gradient near the bottom of Cabeus (a), Haworth (b) and Shoemaker (c). The solid lines denote attenuation coefficient (left Y-axis), and the dashed lines denote thermal gradient (right Y-axis).
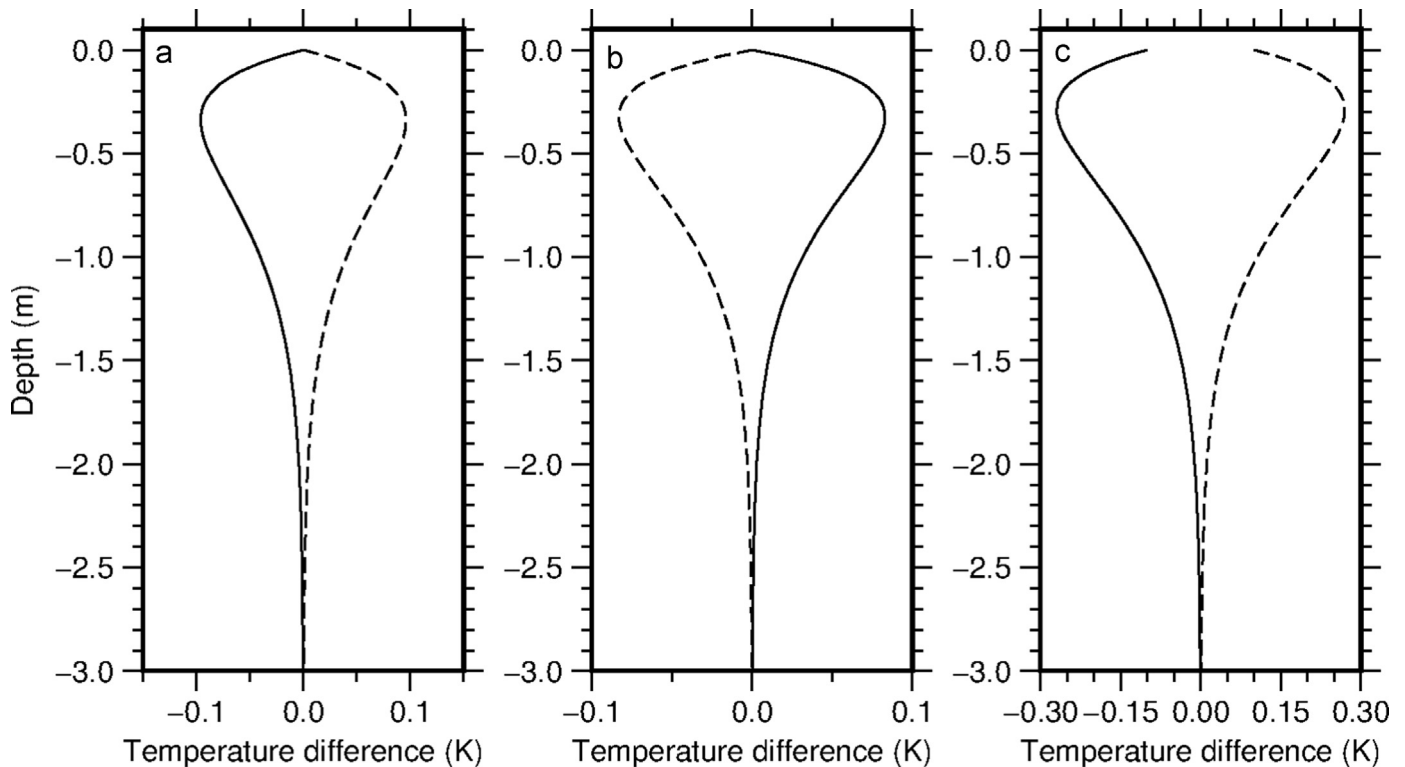

Fig. 10. Differences of maximum (solid lines) and minimum (dashed lines) temperatures between "wet" and dry regolith at Cabeus (a), Haworth (b) and Shoemaker (c).

to observations. The inversion results at LCROSS impact site, for example, changed slightly if both Tb_{37} and Tb_{19} were added by ± 0.5 K. On the other hand, we considered a noise brought only from one channel, namely, $Tb_{37} \pm 0.5$ K or $Tb_{19} \pm 0.5$ K. Fig. 11 shows the inverted minimum and maximum temperature profiles from observation and noise data. Apparently, the temperature difference at surface is less than 4 K, thermal gradients (1–1.1 K/m) and attenuation coefficients (2.8–3.1 m^{-1}) also changed slightly. Similarly, adding the same noise ± 0.5 K to Tb_{19}, we also found that the maximum temperature difference is no more than 4 K,

and their thermal gradients show a similar trend in subsurface. Therefore, observed Tb with < 0.5 K noise have little effect on inverted attenuation coefficient and thermal gradient.

5. Conclusion

Subsurface thermal behavior at cold traps is related to regolith thermophysical properties, water ice content and internal heat flux. In this study, we first constructed daytime Tb_{37} mosaic from
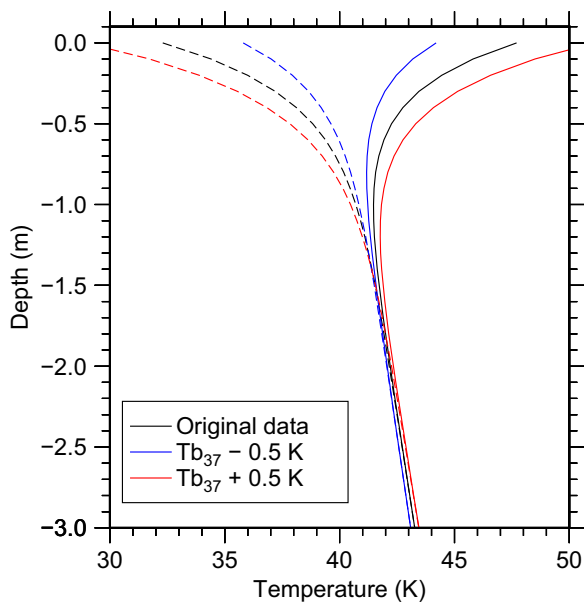
Fig. 11. Comparison of inverted temperature profiles at LCROSS impact site from observation and noise data. The dashed and solid lines denote minimum and maximum profiles, respectively. As an example, a noise ± 0.5 K was added to observed Tb_{37} data.

CE-2 microwave radiometer data at lunar south polar regions ($\geq 80°$S). Extreme low brightness temperature regions, such as Cabeus, Haworth and Shoemaker were well consistent with surface cryogenic regions, CE-1 cold patches and sunlit conditions. Comparing to Tb_{37}, Tb_{19} reveals greater subsurface thermal regime because of its greater penetration depth. Employing Fourier temperature model, we have inverted attenuation coefficients and thermal gradients at Cabeus, Haworth and Shoemaker. The results showed that attenuation coefficients at these craters were inhomogeneous. However, the inverted thermal gradient decreased from walls to the bottom of craters, and this may be related to topographic effect (scattered sunlight).

Considering the continuous supplement of water ice (0%–10%), the attenuation coefficient and thermal gradient varied with the increase of ice content but has small amplitude. It indicated that the mixed ice had little effect on subsurface thermal regime and our inversion results. For large volume of ice (10%) mixed with regolith, the differences of maximum and minimum temperatures between "wet" and dry regolith varied significantly in shallow depth. However, the temperature differences through all depths (0–3 m) were no more than 0.5 K. Thus, subsurface thermal behavior at cold traps investigated by microwave brightness temperature data was mainly dependent on the ice harboring regolith thermophysical properties.

Acknowledgements

References

Arnold, J.R., 1979. Ice in the lunar polar regions. J. Geophys. Res. 84, 5659–5668.

Bills, B.G., Ray, R.D., 1999. Lunar orbital evolution: a synthesis of recent results. Geophys. Res. Lett. 26, 3045–3048.

Chan, K.L., Tsang, K.T., Kong, B., Zheng, Y.C., 2010. Lunar regolith thermal behavior revealed by Chang'E-1 microwave brightness temperature data. Earth Planet. Sci. Lett. 295, 287–291.

Clark, R.N., 2009. Detection of adsorbed water and hydroxyl on the moon. Science 326, 562–564.

Colaprete, A., Schultz, P., Heldmann, J., Wooden, D., Shirley, M., Ennico, K., Hermalyn, B., Marshall, W., Ricco, A., Elphic, R.C., Goldstein, D., Summy, D., Bart, G. D., Asphaug, E., Korycansky, D., Landis, D., Sollitt, L., 2010. Detection of water in the LCROSS ejecta plume. Science 330, 463–468.

Crider, D., Vondrak, R., 2002. Hydrogen migration to the lunar poles by solar wind bombardment of the moon. Adv. Sp. Res. 30, 1869–1874.

Crider, D.H., Vondrak, R.R., 2003. Space weathering effects on lunar cold trap deposits. J. Geophys. Res. 108, 5079.

Evan, S., 1965. Dielectric properties of ice and snow – a review. J. Glaciol. 5, 773–792.

Fang, T., Fa, W., 2014. High frequency thermal emission from the lunar surface and near surface temperature of the Moon from Chang'E-2 microwave radiometer. Icarus.

Feldman, W.C., Lawrence, D.J., Elphic, R.C., Barraclough, B.L., Maurice, S., Genetay, I., Binder, A.B., 2000. Polar hydrogen deposits on the Moon. J. Geophys. Res. 105, 4175–4195.

Feldman, W.C., Maurice, S., Binder, A.B., Barraclough, B.L., Elphic, R.C., Lawrence, D. J., 1998. Fluxes of fast and epithermal neutrons from lunar prospector: evidence for water ice at the lunar poles. Science 281, 1496–1500.

Heiken, G.H., Vaniman, D.T., French, B.M., 1991. The Lunar Sourcebook: A User's Guide to The Moon. Cambridge University Press, New York, pp. 475–552.

Jin, Y.Q., 1984. Wave approach to brightness temperature from a bounded layer of random discrete scatterers. Electromagnetics 4, 323–341.

Keihm, S., Langseth Jr., M., 1973. Surface brightness temperatures at the Apollo 17 heat flow site: thermal conductivity of the upper 15 cm of regolith. In: Lunar and Planetary Science Conference Proceedings, pp. 2503.

Keihm, S., Peters, K., Langseth, M., Chute Jr., J.L., 1973. Apollo 15 measurement of lunar surface brightness temperatures thermal conductivity of the upper 1 1/2 meters of regolith. Earth Planet. Sci. Lett. 19, 337–351.

Klumov, B.A., Berezhnoi, A.A., 2002. Possible origin of lunar ice. Adv. Sp. Res. 30, 1875–1881.

Lucey, P.G., Blasius, K.R., Bussey, B., Hoelter, R.L., Gillis, J.J., Lawson, S.L., Mellon, M., Spencer, J., Urquhart, M., Vasavada, A.R., Wang, A.T., 2004. An imaging radiometer for measurement of lunar polar cold trap temperatures. Proc. SPIE 5660, 98–106.

Meng, Z., Chen, S., Osei, Edward, Matthew, J., Wang, Z., Cui, T., 2010. Research on water ice content in Cabeus crater using the data from the microwave radiometer onboard Chang'e-1 satellite. Sci. China Phys. Mech. Astron. 53, 2172–2178.

Mezger, P.G., Strassl, H., 1959. The thermal radiation of the Moon at 1420 Mc/s. Planet. Sp. Sci. 1, 213–226.

Mitrofanov, I.G., Sanin, A.B., Boynton, W.V., Chin, G., Garvin, J.B., Golovin, D., Evans, L.G., Harshman, K., Kozyrev, A.S., Litvak, M.L., Malakhov, A., Mazarico, E., McClanahan, T., Milikh, G., Mokrousov, M., Nandikotkur, G., Neumann, G.A., Nuzhdin, I., Sagdeev, R., Shevchenko, V., Shvetsov, V., Smith, D.E., Starr, R., Tretyakov, V.I., Trombka, J., Usikov, D., Varenikov, A., Vostrukhin, A., Zuber, M.T., 2010. Hydrogen mapping of the lunar south pole using the LRO neutron detector experiment LEND. Science 330, 483–486.

Noda, H., Araki, H., Goossens, S., Ishihara, Y., Matsumoto, K., Tazawa, S., Kawano, N., Sasaki, S., 2008. Illumination conditions at the lunar polar regions by Kaguya (selene) laser altimeter. Geophys. Res. Lett., 35.

Nozette, S., Lichtenberg, C.L., Spudis, P., Bonner, R., Ort, W., Malaret, E., Robinson, M., Shoemaker, E.M., 1996. The clementine bistatic radar experiment. Science 274, 1495–1498.

Paige, D., Foote, M., Greenhagen, B., Schofield, J., Calcutt, S., Vasavada, A., Preston, D., Taylor, F., Allen, C., Snook, K., Jakosky, B., Murray, B., Soderblom, L., Jau, B., Loring, S., Bulharowski, J., Bowles, N., Thomas, I., Sullivan, M., Avis, C., De Jong, E., Hartford, W., McCleese, D., 2010a. The lunar reconnaissance orbiter diviner lunar radiometer experiment. Sp. Sci. Rev. 150, 125–160.

Paige, D.A., Siegler, M.A., Zhang, J.A., Hayne, P.O., Foote, E.J., Bennett, K.A., Vasavada, A.R., Greenhagen, B.T., Schofield, J.T., McCleese, D.J., Foote, M.C., De Jong, E., Bills, B.G., Hartford, W., Murray, B.C., Allen, C.C., Snook, K., Murray, B.C., Soderblom, L. A., Calcutt, S., Taylor, F.W., Bowles, N.E., Bandfield, J.L., Elphic, R., Ghent, R., Glotch, T.D., Wyatt, M.B., Lucey, P.G., 2010b. Diviner lunar radiometer observations of cold traps in the moon's south polar region. Science 330, 479–482.

Pieters, C., Goswami, J., Clark, R., Annadurai, M., Boardman, J., Buratti, B., Combe, J.P., Dyar, M., Green, R., Head, J., et al., 2009. Character and spatial distribution of oh/ h2o on the surface of the moon seen by m3 on chandrayaan-1. Science 326, 568–572.

Prettyman, T.H., Hagerty, J.J., Elphic, R.C., Feldman, W.C., Lawrence, D.J., McKinney, G.W., Vaniman, D.T., 2006. Elemental composition of the lunar surface: analysis of gamma ray spectroscopy data from lunar prospector. J. Geophys. Res. 111, 1–41.

Reynolds, J., Hough, J., 1957. Formulae for dielectric constant of mixtures. Proc. Phys. Soc. Sec. B 70, 769.

Salvail, J.R., Fanale, F.P., 1994. Near-surface ice on mercury and the moon: a topographic thermal model. Icarus 111, 441–455.

Schorghofer, N., Aharonson, O., 2014. The lunar thermal ice pump. Astrophys. J. 788, 169.

Schorghofer, N., Taylor, G.J., 2007. Subsurface migration of H2O at lunar cold traps. J. Geophys. Res. 112, E02010.

Schultz, P.H., Hermalyn, B., Colaprete, A., Ennico, K., Shirley, M., Marshall, W.S., 2010. The lcross cratering experiment. Science 330, 468–472.

Sefton-Nash, E., Siegler, M., Paige, D., 2013. Thermal extremes in permanently shadowed regions at the lunar south pole. 44, 2617.

Shutko, A.M., Reutov, E.M., 1982. Mixture formulas applied in estimation of dielectric and radiative characteristics of soils and grounds at microwave frequencies. IEEE Trans. Geosci. Remote Sens. GE-20, 29–32.

Siegler, M., Paige, D., Williams, J.P., Bills, B., 2015. Evolution of lunar polar ice stability. Icarus 255, 78–87.

Siegler, M.A., Bills, B.G., Paige, D.A., 2011. Effects of orbital evolution on lunar ice stability. J. Geophys. Res. 116, E03010.

Sunshine, J.M., Farnham, T.L., Feaga, L.M., Groussin, O., Merlin, F., Milliken, R.E., AHearn, M.F., 2009. Temporal and spatial variability of lunar hydration as observed by the deep impact spacecraft. Science 326, 565–568.

Vasavada, A.R., Bandfield, J.L., Greenhagen, B.T., Hayne, P.O., Siegler, M.A., Williams, J.P., Paige, D.A., 2012. Lunar equatorial surface temperatures and regolith properties from the diviner lunar radiometer experiment. J. Geophys. Res., 117.

Vasavada, A.R., Paige, D.A., Wood, S.E., 1999. Near-surface temperatures on Mercury and the Moon and the stability of polar ice deposits. Icarus 193, 179–193.

Watson, K., Murray, B.C., Brown, H., 1961. The behavior of volatiles on the lunar surface. J. Geophys. Res. 66, 3033–3045.

Wessel, P., Smith, W.H., 1991. Free software helps map and display data. Eos Trans. Am. Geophys. Union 72, 441–446.

Wesselink, A., 1948. Heat conductivity and nature of the lunar surface material. Bull. Astron. Inst. Neth. 10, 351–363.

Zheng, Y., Tsang, K., Chan, K., Zou, Y., Zhang, F., Ouyang, Z., 2012. First microwave map of the Moon with Chang'E-1 data: the role of local time in global imaging. Icarus 219, 194–210.

Zhou, M., Zhou, J., Zhang, X., Wang, F., 2010. Inversion of microwave brightness temperature data for estimating lunar regolith thickness. Int. J. Appl. Electromagn. Mech., 33.